# Microstructural stability of secondary phases in an ODS ferritic steel after thermal aging at 873 K

Oñoro, M.; de Castro, V.; Leguey, T.; Pöpperlová, J.; Huizenga, R. M.; Auger, M. A.

**DOI**
10.1016/j.matchar.2023.113517
10.1016/j.matchar.2023.113569

**Publication date**
2024

**Document Version**
Final published version

**Published in**
Materials Characterization

Materials Characterization 207 (2024) 113517

Contents lists available at ScienceDirect

Materials Characterization

journal homepage: www.elsevier.com/locate/matchar

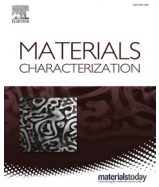

# Microstructural stability of secondary phases in an ODS ferritic steel after thermal aging at 873 K

M. Oñoro [a], V. de Castro [a], T. Leguey [a], J. Pöpperlová [b], R.M. Huizenga [c], M.A. Auger [a,*]

[a] Department of Physics, Universidad Carlos III de Madrid, Av. de la Universidad 30, 28911 Leganés, Madrid, Spain
[b] Steel Institute, RWTH Aachen University (IEHK), Intzestr. 1, 52072 Aachen, Germany
[c] Department of Materials Science and Engineering, Delft University of Technology, Mekelweg 2, 2628 CD Delft, the Netherlands

ARTICLE INFO

*Keywords:*
ODS steel
Aging
Laves phase
Nanoparticles
TEM
APT

ABSTRACT

An oxide dispersion strengthened (ODS) steel with nominal composition Fe–14Cr–2W–0.4Ti–0.3$Y_2O_3$ (wt%) has been manufactured by mechanical alloying of pre-alloyed powders with nanosized $Y_2O_3$, compacted by hot isostatic pressing and hot cross rolled. In order to evaluate the long-term thermal resistance of the alloy, it has been subjected to 2000 h of thermal aging at 873 K, which is a relevant temperature for nuclear reactor applications. A thermodynamic equilibrium simulation indicates the precipitation of Laves phase under the aging parameters used. This prediction is confirmed from the detailed multi-technique characterization performed. Before aging, Ti-rich oxides, Cr-W-rich precipitates ($M_{23}C_6$ type) and a homogeneous Y-rich nanoprecipitate dispersion are observed. After aging, some W-rich precipitates are identified as Laves phase, while $M_{23}C_6$ carbides, Ti-rich oxides and Y-rich nanoprecipitates remain stable. Mechanical characterization performed in a previous research showed higher hardness, a loss of total elongation and a slight shift of the ductile-to-brittle transition temperature (DBTT) towards a higher value after aging, with similar strength values before and after the long-term thermal treatment. These changes can be due to the redistribution of precipitates together with the Laves phase formation. The mechanical properties not being dramatically affected seem to be due to the observed stability of Y-rich nanoprecipitates distribution.

## 1. Introduction

Reduced-activation 9–12%Cr ferritic/martensitic (RAFM) and 12–16%Cr ferritic (RAF) steels have been proposed as candidates to be used as structural materials in fusion power systems over the last decades, due to their high resistance to radiation induced effects like swelling, He embrittlement or irradiation creep at high temperatures [1–5]. Both steel types are interesting for nuclear applications, even though the operational temperature of RAFM steels is lower than the one for RAF steels [6]. One possibility to improve the already good properties of these materials is by adding a dispersion of nano-oxides during the manufacturing process to produce what is called oxide dispersion strengthened (ODS) steels, which are among the most promising structural materials to be used in future fusion reactors [7–9]. The ODS material is based on the presence of a homogeneous distribution of stable oxide nanoparticles [10–13] in the steel. $Y_2O_3$ is one of the oxide candidates that has shown the best performance in ODS steel manufacturing [12]. The addition of titanium to the alloy promotes a finer nanoparticle dispersion of Y-Ti-O complex oxides [14,15] providing high tensile strength and good ductility up to 1073 K [16,17]. In these steels, the nanometric particles act as recombination centers for point defects that might form under irradiation [18,19] improving, as a result, the materials performance under the harsh operation conditions that they need to withstand inside the reactor, including irradiation, stress, and pressure at high temperatures.

Several manufacturing routes have been explored over the last decades in order to successfully produce ODS RAFM/RAF steels at laboratory scale and at semi-industrial scale. These routes typically involve powder metallurgy processes, such as mechanical alloying, followed by a consolidation process: hot isostatic pressing or hot rolling, combined with thermomechanical treatments [13]. The microstructure and mechanical properties of the alloys obtained by these routes are currently well known; it has been observed that the maximum potential operating temperatures for ODS RAF steels can go up to 1073 K or higher, offering superior high-temperature thermal creep strength and increased oxidation/corrosion resistance [20]. In order to keep improving the

* Corresponding author at: Department of Physics, Universidad Carlos III de Madrid, Avenida Universidad 30, 28911 Leganés, Madrid, Spain.
*E-mail address:* mauger@fis.uc3m.es (M.A. Auger).

https://doi.org/10.1016/j.matchar.2023.113517
Received 2 August 2023; Received in revised form 24 November 2023; Accepted 25 November 2023
Available online 29 November 2023

general performance of ODS steels and increase their applications range, new production routes such as STARS (Surface Treatments of gas Atomized powder followed by Reactive Synthesis) [21], SolidSTIR™ [22] or additive manufacturing [23] are currently being explored and validated; they offer very promising outcomes as possibilities to successfully produce fuel cladding tubes.

In order to evaluate the long-term stability of ODS steels at the high temperatures that they will have to withstand inside the reactor, in the 623 K–823 K range or higher [24,25], it is essential to perform thermal aging experiments at relevant temperatures, and identify any microstructural changes that may affect the mechanical properties and general performance of the materials. Long-term aging in steels can produce dissolution of already existing precipitates, segregation of elements to grain boundaries and, eventually, precipitation of new phases, like α' precipitation [26] or Laves phase formation ($(Fe,Cr)_2W$) [27], which may be detrimental to the mechanical performance. Some works have analyzed the microstructural and mechanical changes in RAFM steels after aging [27–30], but the number of studies performed in ODS Fe-14Cr (wt%) steels is quite limited [31]. The aim of this work is to provide experimental data on thermal aging experiments performed at relevant temperatures on ODS Fe-14Cr (wt%) steels.

The mechanical properties of the alloy presented in this work have been already reported in [32,33]. The aging treatment produced an increase in hardness, almost no change on the yield and tensile strength values but a general reduction of the total elongation. Additionally, the ductile-to-brittle transition temperature (DBTT) slightly shifted towards a higher temperature. These changes in the mechanical properties may be due to the redistribution and evolution of secondary phases, while the yield and tensile strength stability may be related to the nanoparticle dispersion. The present work aims to further research this aspect, by predicting and analyzing the microstructure of an ODS steel before and after being submitted to a thermal aging treatment at 873 K for 2000 h.

## 2. Materials and methods

The ODS ferritic alloy was manufactured by mechanical alloying of pre-alloyed atomized Fe–14Cr–2W–0.4Ti (wt%) powder with $0.3Y_2O_3$ (wt%) nanosized powder in a planetary ball mill, using austenitic steel vessels and balls, at 300 rpm in $H_2$ atmosphere for 27 h with a ball-to-powder ratio of 10:1. The chemical composition of the alloyed powder is listed in Table 1. The milled powder was packed into mild-steel cans, degassed at 693 K for 24 h, sealed and consolidated by hot isostatic pressing (HIP) at 175 MPa and 1373 K for 2 h. The obtained material was subsequently hot cross rolled (HCR) at 1423–1473 K for 18 to 20 passes, rotating the sample 90° after each pass, reaching ~70% thickness reduction. Following HCR, the material was annealed at 1273 K for 2 h and air cooled. The material at this stage is taken as a reference, and it will be denoted as ODS reference. Subsequently, one batch of the alloy was thermally aged at 873 K for 2000 h in Ar atmosphere and air cooled. This material will be denoted as ODS aged. Further details regarding the manufacturing process can be found elsewhere [32,34].

The thermodynamic modelling software ThermoCalc®, based on the CALPHAD method [35], was used for calculating the phase equilibria in the ODS steel, in order to predict possible secondary phases formation and their thermal stability. All presented thermodynamic calculations were performed utilizing the Thermo-Calc Software TCFE10 Steels/Fe-alloys database, including the element yttrium and using the chemical composition listed in Table 1.

X-ray diffraction data were acquired in a Bruker-AXS D8 diffractometer in Bragg-Brentano geometry, using Cu $K_\alpha$ radiation, operating at 45 kV and 40 mA at a step size of 0.015° in 2θ and using 2 s as counting time per step with a LynxEye XE-T detector. Electron backscatter diffraction measurements (EBSD) were performed in a TENEO-FEI scanning electron microscope using an AMETEK EDAX Velocity™ Pro camera. Phase orientation identification was determined using the EDAX APEX™ software.

Specimens for transmission electron microscopy (TEM) characterization were prepared from 3 mm diameter disks, electropolished in a TENUPOL-5 twin-jet polisher using 5 (vol%) $HClO_4$ + 95(vol%) $CH_3OH$ as electrolyte. Prior to each TEM observation session, the disks were additionally plasma cleaned for 5 min.

A Philips Tecnai F20 and a Talos F200X FEI TEM, both operating at 200 kV were used for TEM imaging and data acquisition. Digital-Micrograph® software [36] and ImageJ software [37] were used for data analysis.

ODS reference specimens for atom probe tomography (APT) characterization were prepared by using the focused ion beam (FIB) lift-out technique [38] in a Zeiss Auriga 40 FIB/SEM. ODS aged specimens for APT were prepared by following a standard two-stage electro-polishing method [39,40]. Both methods yielded needle shaped samples with a final radius apex below 100 nm. APT analysis was carried out in a CAMECA LEAP™ 5000XR operating in laser (wavelength of 355 nm) pulsing mode, at a repetition rate of 200 kHz and a laser energy of 0.040 nJ. The specimen base temperature was around 50 K. High quality datasets containing 4 and 60 million ions were obtained for the ODS reference and for the ODS aged samples, respectively. CAMECA IVAS® 3.8.10 commercial software [41] was used for data analysis and reconstruction.

## 3. Results

### 3.1. Thermodynamic equilibrium simulation

The calculated diagram for phase fractions obtained from the ThermoCalc simulation for the ODS steel is displayed in Fig. 1(a), which shows the stability of the occurring phase constituents as a function of temperature in the relevant 773–1273 K range, in which the investigated ODS steel exhibits a fully ferritic structure including oxides, carbides/nitrides and intermetallic phases. Based on the designation of the implemented TCFE10 database and the calculated chemical composition of the phases, yttrium oxide ($Y_2O_3$), titanium oxide ($Ti_2O_3$), carbides/nitrides (M(C,N) and $M_{23}C_6$) and Laves phase ($(Fe,Cr)_2W$) are identified. Regarding the applied thermal aging at 873 K for 2000 h, all named secondary phases are present in equilibrium and are, therefore, relevant. The calculated dissolution temperatures as well as the phase mole fraction of the occurring phases at 873 K are summarized in Table 2. The equilibrium M(C,N) precipitates can be classified either as titanium carbides/nitrides or titanium carbonitrides. The M(C,N) precipitates can probably be formed during the pre-alloying processing. The $M_{23}C_6$ carbides exhibit a combined chemical composition of M=Fe, Cr, W. The complete calculated chemical compositions at 873 K of the secondary phases M(C,N), $M_{23}C_6$, Laves phase ($(Fe,Cr)_2W$), as well as of the ferritic matrix are shown in Fig. 1(b).

### 3.2. X-ray diffraction and EBSD measurements

Fig. 2(a) and Fig. 2(b) show the XRD patterns for the ODS reference and the ODS aged materials, respectively. It can be seen that both patterns display a BCC α phase (14754 file in the FIZ Karlsruhe-ICSD database [42]). The peaks are mainly sharp, this aspect being

**Table 1**
Chemical composition (in wt%) of the ODS steel alloyed powder [34].

| Fe | Cr | W | Ti | Y | O | C | Al | N | Si | S |
|---|---|---|---|---|---|---|---|---|---|---|
| Bal. | 13.1 | 2.0 | 0.38 | 0.18 | 0.17 | 0.04 | < 0.05 | 0.020 | < 0.05 | < 0.03 |

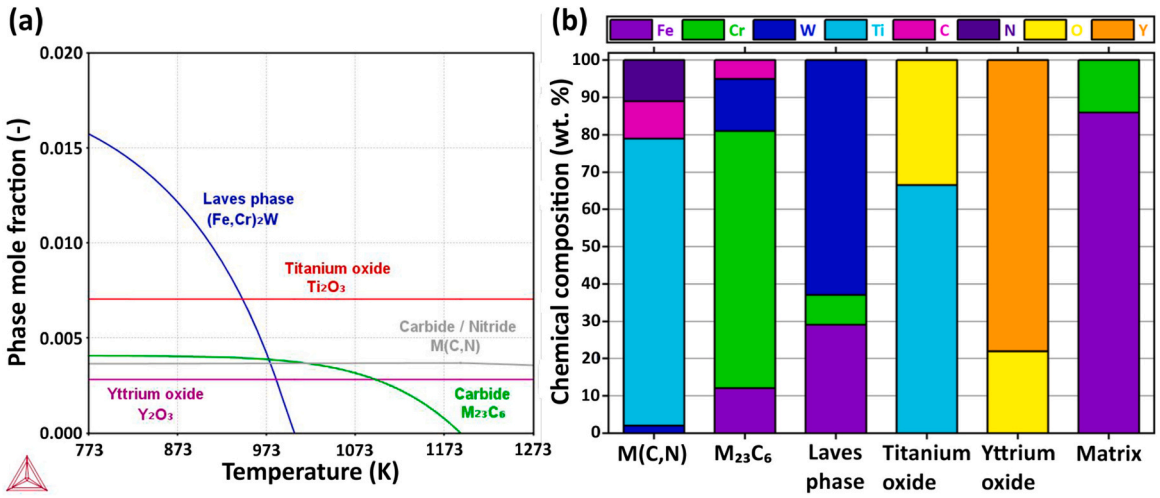


**Fig. 1.** Results of thermodynamic equilibrium calculation of the ODS steel utilizing ThermoCalc®, TCS steel database TCFE10. (a) Calculated mole fraction of the secondary phases identified in the ODS steel ferritic matrix as a function of temperature and (b) calculated chemical composition of all the phases at 873 K.

**Table 2**
Calculated dissolution temperature and phase mole fraction of secondary phases occurring in the ODS steel at 873 K, utilizing ThermoCalc®, TCS steel database TCFE10.

| Secondary phase | Carbide / nitride M(C,N) | Carbide $M_{23}C_6$ | Laves phase $(Fe,Cr)_2W$ | Titanium oxide $Ti_2O_3$ | Yttrium oxide $Y_2O_3$ |
|---|---|---|---|---|---|
| Dissolution temperature (K) | 1788 | 1190 | 1003 | 2045 | 1459 |
| Phase mole fraction (−) at 873 K | 0.004 | 0.004 | 0.012 | 0.007 | 0.003 |

associated to a low number of defects and large crystallites (larger than 100 nm). The lattice parameter of the two samples appears to differ slightly: 2.8737±0.0001 Å for ODS reference and 2.8724±0.0001 Å for ODS aged. In the aged material, the presence of two low intensity peaks can be seen at $\theta \approx 38^o$ and $\theta \approx 41.7^o$, not present in the reference material (Fig. 2(c)). These peaks match a Laves phase structure (155757 file in the FIZ Karlsruhe-ICSD database [43]).

EBSD point analysis was performed on specific precipitates before and after aging; an example of representative precipitates analyzed on the ODS reference sample and on the ODS aged sample can be seen in Fig. 3(a) and Fig. 3(b), respectively. A minimum value of 0.1 was set for the confidence index (CI), to ensure accurate crystallographic indexation. The crystal structure of six different precipitates in the ODS reference sample matched the $M_{23}C_6$ pattern as in Fig. 3(d); Laves phase

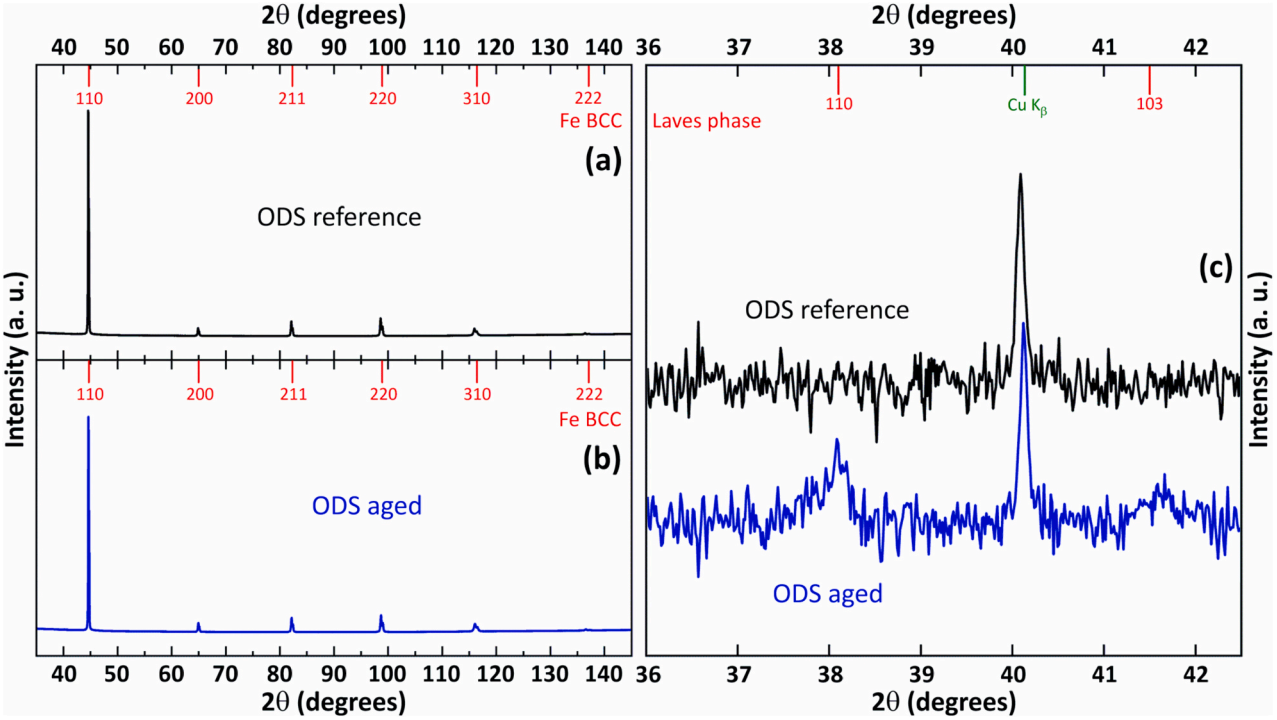


**Fig. 2.** XRD patterns from (a) the ODS reference material and (b) the ODS aged material. (c) Zoomed in XRD pattern from (a) and (b). The diffracting lattice planes and the Cu $K_\beta$ emission line are indicated at the upper axes.

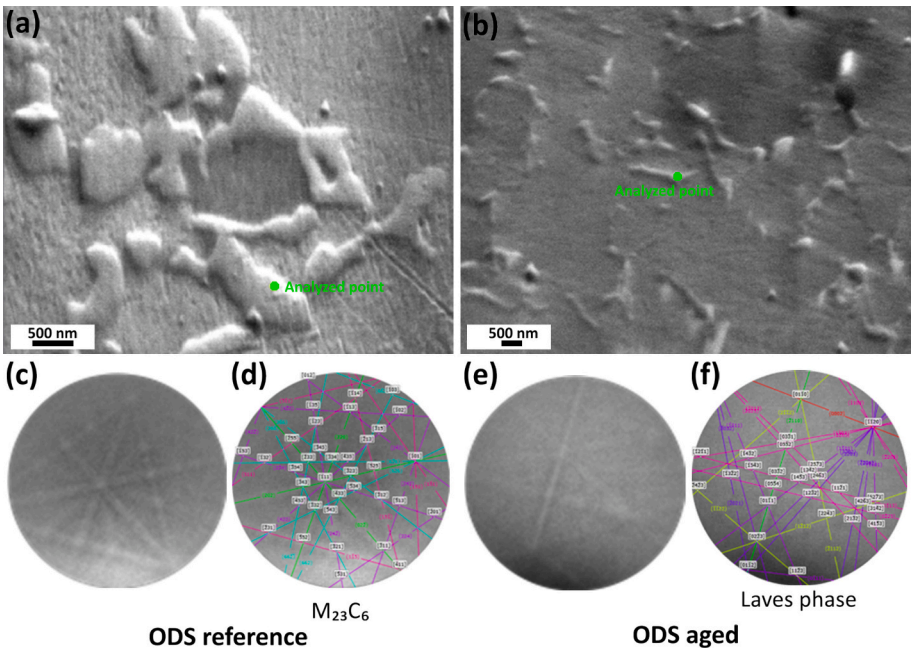


**Fig. 3.** SEM images of (a) the ODS reference sample and (b) the ODS aged sample. (c) EBSD pattern obtained from the point highlighted in (a). (d) Indexation as $M_{23}C_6$ of the pattern displayed in (c). (e) EBSD pattern obtained from the point highlighted in (b). (f) Indexation as Laves phase of the pattern displayed in (e).

was not found in this case. In the ODS aged sample, the crystal structure of two precipitates was identified as $M_{23}C_6$ (similar pattern as in Fig. 3 (d), not shown in this case) while other two were identified as Laves phase ($Fe_2W$), as displayed in Fig. 3(f).

### 3.3. TEM characterization of secondary phases

#### 3.3.1. ODS reference material

Previous studies performed on this same ODS steel show that three types of secondary phases coexist: Ti-rich oxides, Y-rich nano-precipitates and Cr-W-rich precipitates [32,44].

Scanning transmission electron microscopy (STEM) images and Energy-dispersive X-ray spectroscopy (EDS) chemical maps of some of these precipitates are shown in Fig. 4. The EDS maps show Ti-Cr-rich oxides with round morphology and sized between 20 nm and 400 nm. These oxides were mainly found near grain boundaries. As it can be seen in Fig. 4(c), a Cr-rich shell appears to surround some of them. A homogeneous distribution of very small Y-rich nanoprecipitates (95% of them being smaller than 5 nm in size) can be observed in Fig. 4(h) and in Fig. 5(a), some of the larger ones attached to Ti-Cr oxides. A size histogram for the Y-rich nanoprecipitates is displayed in Fig. 10(a). The statistics, obtained from the analysis of several images, are summarized in Table 3. The Cr-W-rich precipitates have already been characterized in [32]. They are found to be irregularly shaped, up to 600 nm in size and mainly located along grain boundaries. To complete their characterization, high-resolution imaging has been performed (Fig. 5(b)). Fig. 5(c) displays the EDS spectra of the precipitate shown in Fig. 5(b), which confirms its Cr-W-rich composition. The crystal structure of the precipitate shown in Fig. 5(b) has been determined [45] from the microdiffraction pattern ([–1–2 7] zone axis) displayed in Fig. 5(d), being identified as $M_{23}C_6$ carbide type.

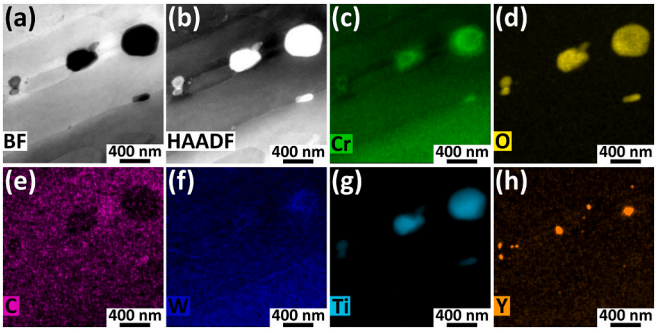


**Fig. 4.** STEM images of the ODS reference sample. (a) BF image, (b) High-angle annular dark-field (HAADF) image, (c) Cr (K) map, (d) O (K)map, (e) C (K) map, (f) W (M) map, (g) Ti (K) map and (h) Y (L) map.

#### 3.3.2. ODS aged material

The stability of the Ti-rich oxides was already assessed in [32], finding a slight coarsening from 100±50 nm to 110±80 nm and a slight Ti content increase after aging. In [32] it was observed an increase in the W content of the Cr-W-rich precipitates after aging. In the present study, the effect of the aging process on the Cr-W-rich precipitates and the Y-rich nanoparticles has been investigated. Fig. 6, Fig. 7 and Fig. 8 show STEM images and EDS chemical maps of different regions in the ODS aged material. Most of the Cr-W-rich precipitates shown in Fig. 6 are elongated and do not appear to contain C (Fig. 6(c), Fig. 6(e) and Fig. 6 (f)). One isolated Cr carbide without W (Fig. 6(c), Fig. 6(e) and Fig. 6(f)) and some Ti oxides (Fig. 6(d) and Fig. 6(g)) are also visible in this region. Fig. 7 shows another area, containing many Ti oxides (Fig. 7(d) and Fig. 7(g)) together with some elongated Cr-W-rich precipitates that again appear to be free of C (Fig. 7(c), Fig. 7(e) and Fig. 7(f)). However, in the region depicted in Fig. 8, some Cr-W-rich precipitates do contain C (Fig. 8(c), Fig. 8(e) and Fig. 8(f)). It is worth mentioning that, in this case, their shape is more irregular than in the regions displayed in Fig. 6 and in Fig. 7. These analyses suggest that, although some Cr-W carbides remain after the aging process, a new Cr-W-rich phase has precipitated. A high number of Y-rich nanoprecipitates can be intuited in Fig. 6(h), Fig. 7(h), Fig. 8(h), being more evident in Fig. 9(a). A size histogram for the Y-rich nanoprecipitates in the ODS aged material, obtained from the analysis of several images, is displayed in Fig. 10(b). The statistics obtained from those histograms are summarized in Table 3, together with the results obtained for the ODS reference material.

The crystal structure of the Cr-W-rich precipitates that appear to be free of C has been determined from high-resolution electron microscopy (HREM) analyses [45], showing that it is compatible with $WFe_2$ or W(Fe,

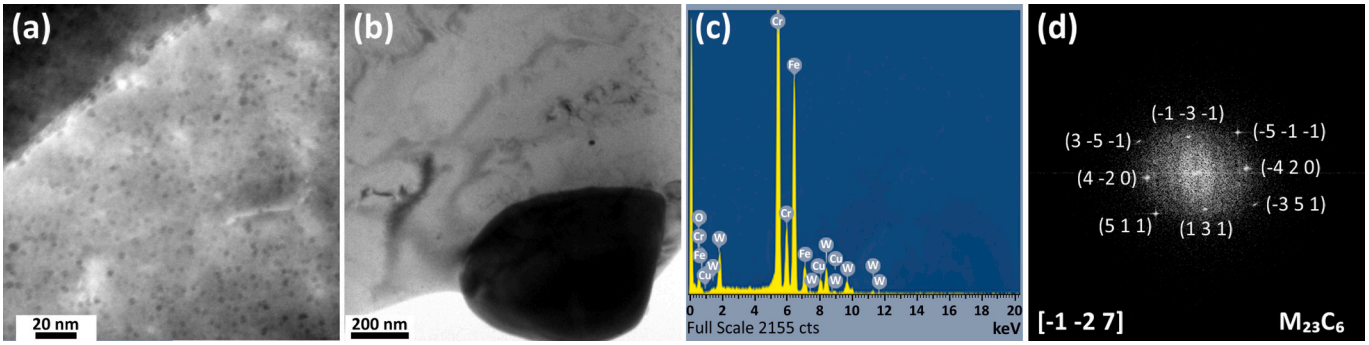


**Fig. 5.** (a) HAADF image showing the homogeneous dispersion of Y-rich nanoprecipitates and (b) BF-TEM image showing a Cr-W-rich precipitate in the ODS reference material. (c) EDS spectra of the precipitate in (b). The Cu peaks in the spectrum come from the Cu grid used to transfer the sample into the TEM instrument. (d) Electron microdiffraction pattern from the precipitate in (b), indexed as $M_{23}C_6$ in zone axis [–1–2 7].

**Table 3**
Summary of the measurements performed by TEM analyses on the Y-rich nanoprecipitates.

| Sample | Number of precipitates analyzed | Size range (nm) | Average size (nm) | Median size (nm) |
|---|---|---|---|---|
| ODS reference | 456 | 1–25 | 3±2 | 2.20 |
| ODS aged | 250 | 1.5–10 | 3±1 | 2.65 |

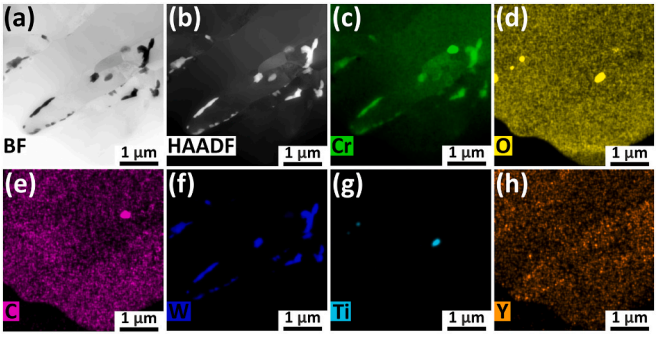


**Fig. 6.** STEM images of the ODS aged sample. (a) BF image, (b) HAADF image, (c) Cr (K) map, (d) O (K) map, (e) C (K) map, (f) W (M) map, (g) Ti (K) map and (h) Y (L) map.

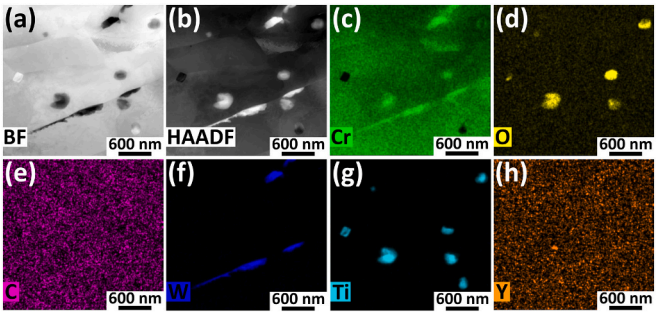


**Fig. 7.** STEM images of the ODS aged sample. (a) BF image, (b) HAADF image, (c) Cr (K) map, (d) O (K) map, (e) C (K) map, (f) W (M) map, (g) Ti (K) map and (h) Y (L) map.

$Cr)_2$ Laves phase. Fig. 9(b) displays a TEM image of an elongated W-rich precipitate located at a grain boundary in the ODS aged material. Fig. 9 (c) displays the EDS spectra of the precipitate highlighted in Fig. 9(b), compatible with Laves phase composition. Fig. 9(d) shows the electron

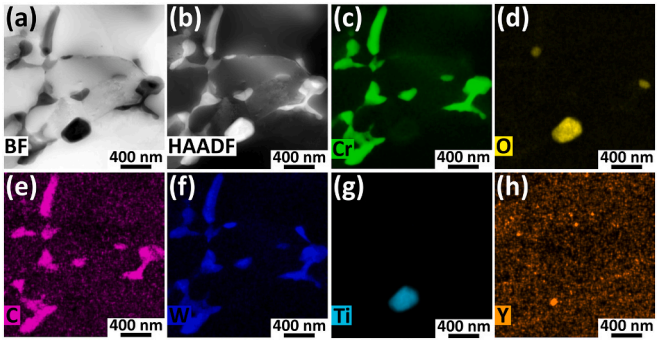


**Fig. 8.** STEM images of the ODS aged sample. (a) BF image, (b) HAADF image, (c) Cr (K) map, (d) O (K) map, (e) C (K) map, (f) W (M) map, (g) Ti (K) map and (h) Y (L) map.

microdiffraction pattern of the precipitate highlighted in Fig. 9(b), whose indexation in [0 1 0] zone axis,confirms its structure as a Laves phase precipitate. Furthermore, the streaked diffraction spots observed in Fig. 9(d) are typically mentioned in the literature as characteristic of Laves phase presence [46–49]. These results confirm that, although some Cr-W carbides remain after the aging process, Laves phase precipitated.

### 3.4. APT characterization

APT reconstructed volumes for the ODS reference and the ODS aged materials are displayed in Fig. 11(a) and Fig. 11(b), respectively. The analyzed volumes correspond to regions inside grains; no grain boundaries could be observed and, as a consequence, none of the Cr-W-rich precipitates, observed by TEM to be mainly located at grain boundaries, could be characterized by APT. Y-Ti-O nanoclusters were found homogeneously distributed inside the analyzed volumes. Average compositional measurements of the bulk volume and the matrix (bulk volume minus Y-Ti-O nanoclusters volume) are summarized in Table 4.

The first nearest neighbor (1NN) distance distribution [50] of Cr-Cr, W-W and Y-YO-TiO ions was calculated for the ODS reference and ODS aged samples, and shown in Fig. 12. It can be seen that no clustering of Cr or W ions was detected in any of the samples as their actual distributions match a random distribution, indicating that Cr-W-rich precipitates, $M_{23}C_6$ or Laves phase, did not precipitate and that α' phase formation was not detected in the analyzed volumes. Y, YO and TiO ions do form precipitates, as the actual distribution of first nearest neighbors differs from a random distribution. Clustering of these ions can also be seen in the 3D ion map reconstructions displayed in Fig. 11.

Y, YO and TiO ions defined nanoprecipitates, and were selected as solute ions for cluster analysis. Cluster analysis was performed by

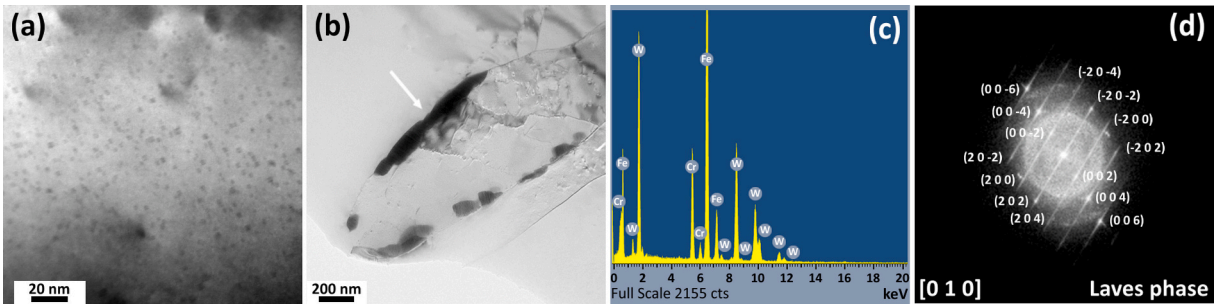


**Fig. 9.** (a) HAADF image showing the homogeneous dispersion of Y-rich nanoprecipitates and (b) BF-TEM image showing a Cr-W-rich precipitate (white arrow) in the ODS aged material. (c) EDS spectra of the precipitate highlighted in (b). (d) Electron microdiffraction pattern from the precipitate highlighted in (b), identified as Laves phase in zone axis [0 1 0].

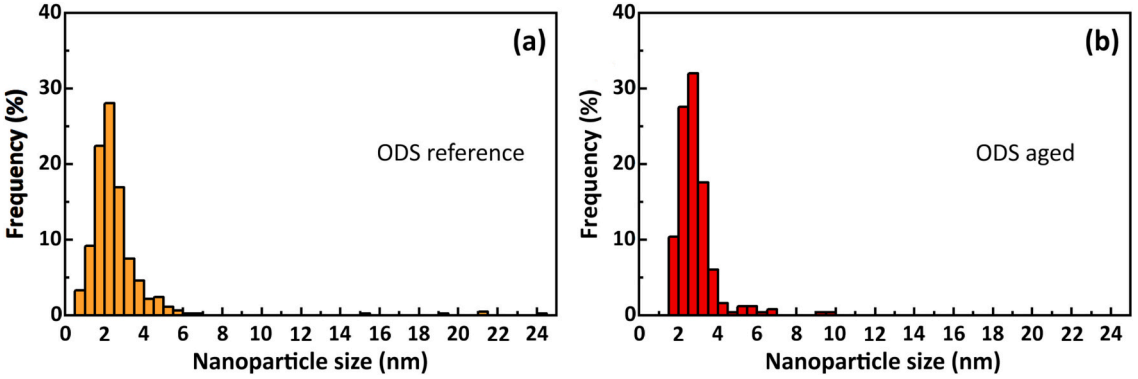


**Fig. 10.** Y-rich nanoprecipitates size distribution histogram in (a) the ODS reference material and in (b) the ODS aged material.

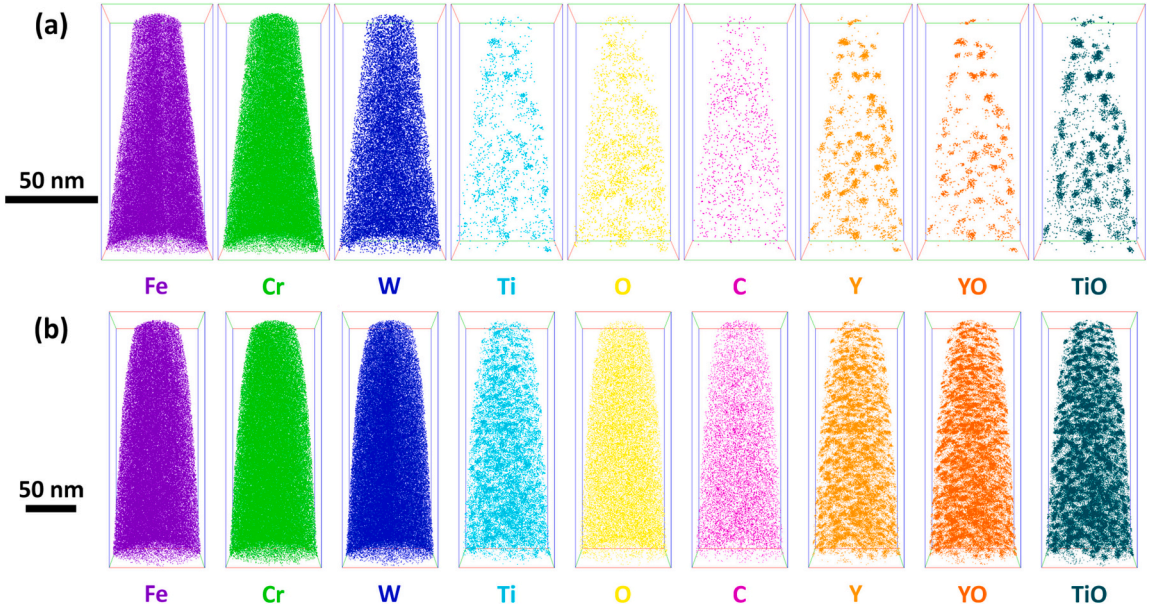


**Fig. 11.** 3D APT ion map reconstructions for (a) ODS reference and (b) ODS aged materials.

implementing the maximum separation method [51] according to the criteria developed in [52]. The cluster size was calculated as the Guinier diameter, i.e. twice the Guinier radius [53]. The Guinier diameter histograms for the ODS reference and the ODS aged materials are displayed in Fig. 13(a) and Fig. 13(b), respectively. The cluster volume was calculated as the volume of a Guinier-radius sphere. The distance between clusters was taken as the average distance from the center of mass [54] of one cluster and the center of mass of its first neighbor. The number density of clusters was calculated as the number of clusters present in the APT reconstructed volume divided by the analyzed volume. The volume fraction of clusters is calculated as the number of ions inside clusters divided by the total number of ions in the reconstructed volume. A summary of the APT cluster analysis is displayed in Table 5.

**Table 4**
Bulk and matrix composition of the ODS reference and ODS aged materials obtained by APT analysis.

| | Bulk composition | | Matrix composition | |
|---|---|---|---|---|
| | ODS reference | ODS aged | ODS reference | ODS aged |
| Ion type | (wt%) | (wt%) | (wt%) | (wt%) |
| Fe | 83.2±0.4 | 82.9±0.5 | 83.4± 0.7 | 83.5±0.4 |
| Cr | 13.49±0.05 | 13.11±0.04 | 13.51± 0.08 | 13.07±0.10 |
| W | 2.32±0.02 | 1.71±0.26 | 2.33±0.01 | 1.71±0.25 |
| Ti | 0.21±0.05 | 0.42±0.04 | 0.17±0.11 | 0.30±0.06 |
| Y | 0.23±0.03 | 0.28±0.00 | 0.13±0.13 | 0.06±0.02 |
| O | 0.25±0.08 | 0.40±0.04 | 0.23±0.10 | 0.16±0.02 |
| N | 0.07±0.04 | 0.11±0.02 | 0.07±0.04 | 0.11±0.01 |
| C | 0.01±0.00 | 0.06±0.01 | 0.01±0.00 | 0.06±0.01 |
| Si | 0.04±0.00 | 0.03±0.01 | 0.05±0.00 | 0.03±0.00 |
| S | 0.00 | 0.00±0.00 | 0.00±0.00 | 0.03±0.00 |
| Al | 0.00 | 0.00±0.00 | 0.00±0.00 | 0.00±0.00 |
| As | 0.02±0.02 | 0.00±0.00 | 0.04±0.02 | 0.01±0.00 |
| P | 0.00±0.00 | 0.00±0.00 | 0.00±0.00 | 0.00±0.00 |
| Mn | 0.04±0.00 | 0.28±0.05 | 0.04±0.00 | 0.29±0.05 |
| V | 0.07±0.00 | 0.68±0.11 | 0.07±0.00 | 0.68±0.10 |

## 4. Discussion

In a previous research [32], three types of precipitates were observed in the investigated ODS steel: Cr-W-rich, Ti-rich and Y-rich precipitates. These observations agree with the thermodynamic equilibrium simulation results (Fig. 1 and Table 2), which indicate the presence of those phases.

It has been reported that M(C,N) precipitates can form easily in a ferritic matrix with a Ti concentration higher than 0.002 wt% [55]. Also, a preferred precipitation of carbides during the manufacturing process can be expected, which is confirmed by TEM observation (Fig. 4). The observed irregular precipitates exhibiting high Cr and W content may correspond to $M_{23}C_6$ carbides. $M_{23}C_6$ precipitates have been identified by microdiffraction (Fig. 5) in the ODS reference material and by point EBSD analysis in both the ODS reference and the ODS aged materials (Fig. 3). The precipitation of a high number of carbides during the processing results in a significant depletion of C in the microstructure, especially nearby the area of the grain boundaries. For instance, the Cr-W-rich precipitates observed at the grain boundaries in Fig. 6 and Fig. 7 do not contain any C. Cr and W generally exhibit a high C affinity; therefore, the formation of the carbides can be seen as a process concurrent to a possible precipitation of the Laves phase. Laves phase formation at grain boundaries has been widely observed in long-term aged steels and Fe-based alloys [27,46–49,56,57], as W is likely to segregate to grain boundaries and this effect is further favored by the long-term aging treatment. When W concentration is high and beyond the accommodation of the grain boundaries, the Laves-phase will begin to precipitate. Laves phase precipitates are coherent with a grain but their growth is incoherent into the adjacent grain; their growth is, therefore,

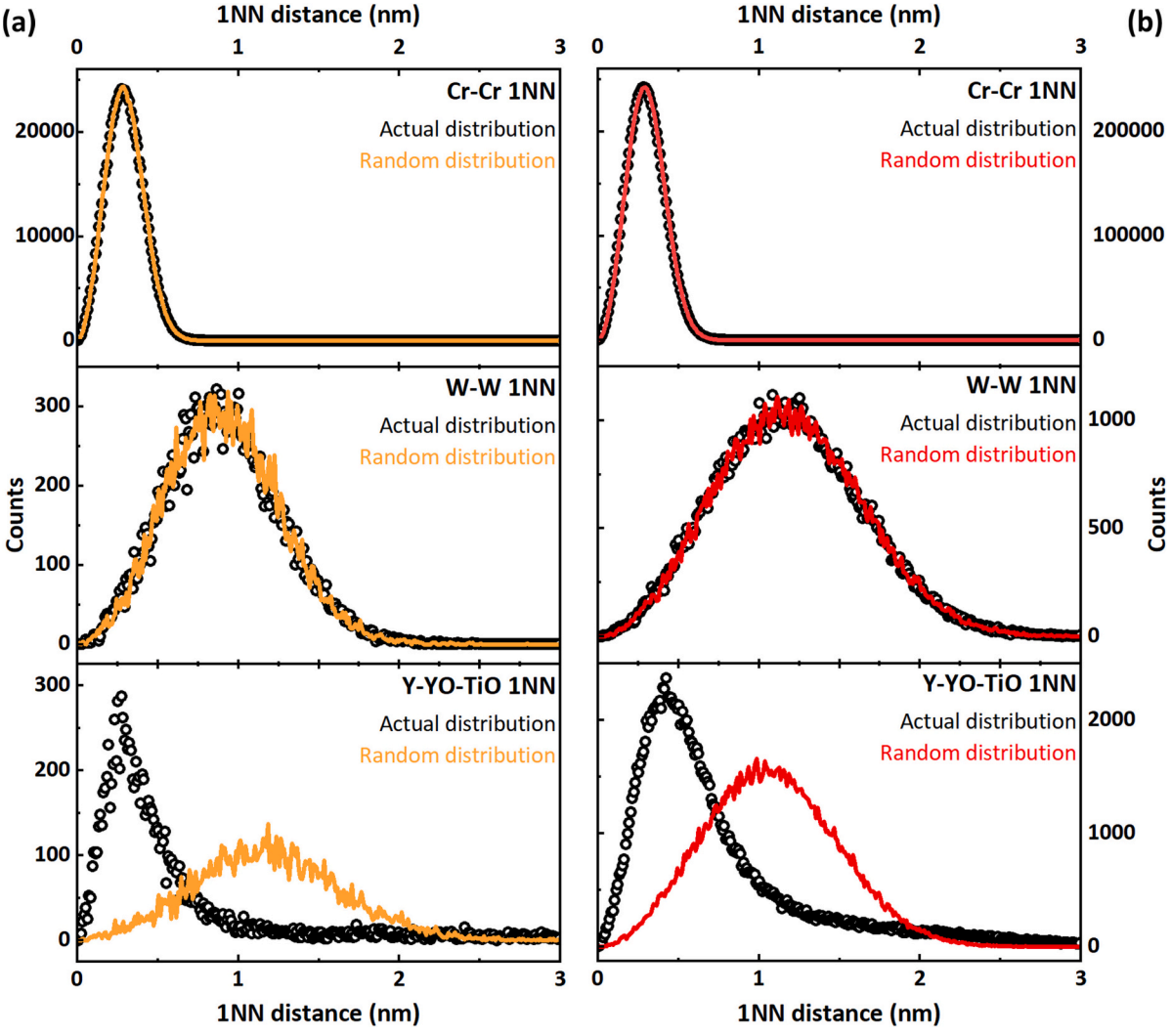


**Fig. 12.** First Cr-Cr, W-W and Y-YO-TiO nearest-neighbor distance distributions in (a) ODS reference and (b) ODS aged materials.

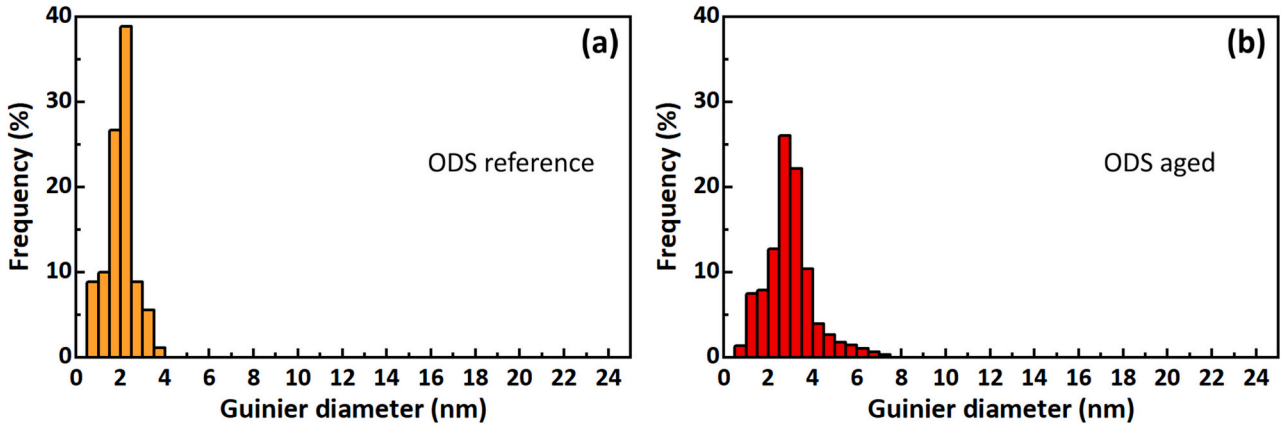


**Fig. 13.** APT Guinier diameter histograms for (a) the ODS reference material and (b) the ODS aged material.

**Table 5**
Summary of APT cluster analysis results.

| | ODS reference | ODS aged |
|---|---|---|
| Number of clusters analyzed | 90 | 972 |
| Size range (nm) | 0.7–3.6 | 0.7–7.2 |
| Average Guinier diameter (nm) | 2.0±0.6 | 2.9±1.1 |
| Average volume ($nm^3$) | 5.4±4.5 | 17.1±5.0 |
| Distance between 1st neighbor clusters (nm) | 8±2 | 8±2 |
| Number density ($m^{-3}$) | $2.1 \cdot 10^{24}$ | $1.5 \cdot 10^{24}$ |
| Volume fraction (%) | 0.5 | 1.4 |
| | Cluster composition | |
| Y (at. %) | 34.1±8.6 | 31.2±6.6 |
| Ti (at. %) | 25.7±6.3 | 28.3±5.8 |
| O (at. %) | 40.2±3.5 | 40.5±2.6 |
| Y/Ti | 1.6±1.1 | 1.2±0.7 |
| (Y + Ti)/O | 1.5±0.2 | 1.5±0.2 |

heterogeneous [57]. According to basic principles in phase transformations in alloys [58], it is believed that coherent interfaces have low mobility while incoherent interfaces have high mobility; and therefore, incoherent interfaces could grow into the grain with which there is no rational orientation relationship. The behavior of the nucleation and growth of Laves precipitates at grain boundaries can be explained in this way [46,57]. In the present study, Laves phase precipitation can happen during the thermal aging at 873 K due to its temperature stability, as can be seen in the ThermoCalc simulation results summarized in Table 2. Also, the high availability of W due to the 2.0 wt% initial content in the alloy, the position at the grain boundaries being favorable for W diffusion and the increased W content observed in some precipitates [32], support the possibility of Laves phase formation. The elemental chemical composition considered to perform the thermodynamic simulation corresponds to the alloyed powder (Table 1). ThermoCalc simulation assumes thermodynamic equilibrium after interminable slow cooling. In the present case, HCR is not an equilibrium process, but the subsequent thermal aging is definitely an equilibrium one. The thermodynamic simulation predicts that the elemental chemical composition of the alloyed powder does promote Laves phase formation at the aging temperature studied. This prediction is experimentally confirmed, as Laves phase has been experimentally observed in the ODS aged material by XRD (Fig. 2(c)), EBSD point analysis (Fig. 3(f)) and TEM diffraction analysis of precipitates located at grain boundaries (Fig. 9(c)). The slightly smaller lattice parameter measured by XRD in the ODS aged sample respect of the ODS reference one, might be related to the diffusion of W (large atom) out from the matrix and into precipitates, leading to a smaller lattice parameter. This is supported by APT analysis, as bulk and matrix composition inside grains (Table 4) shows a lower W content in the ODS aged material with respect to the ODS reference one, suggesting W enrichment in other regions like grain boundaries and/or precipitates, in agreement with the increased W content observed in some precipitates [32]. Also, no α' or W-rich precipitates were found in the volumes analyzed by APT.

Stability of Ti oxides is predicted by the thermodynamic equilibrium simulation (Fig. 1 and Table 2) and confirmed by TEM observation before aging (Fig. 4) and after aging (Fig. 6, Fig. 7 and Fig. 8). Y-rich nanoprecipitates homogeneously distributed inside grains before and after aging were found by TEM (Fig. 5(a) and Fig. 9(a), respectively) and by APT (Fig. 11). The average size of the nanoprecipitates measured by TEM was similar before and after aging, but the median size was slightly larger after aging (Table 3). From APT measurements, an increase in size after aging, reflected in an increased volume fraction and reduced number density could be seen (Table 5), suggesting dissolution of some nanoprecipitates in favor of the growth of existing ones. The distance between first neighbor clusters and the composition of the nanoprecipitates in terms of the (Y+Ti)/O ratio remained unchanged after aging, suggesting stability of the nanoparticle dispersion. The thermodynamic equilibrium simulation confirmed the stability of yttrium oxide and titanium oxide (Fig. 1 and Table 2), which may be extended to confirm the experimentally observed stability of the Y-Ti-O clusters. The thermal stability of Y-rich nanoprecipitates has also been reported in the literature [59,60].

The mechanical properties of these materials were analyzed in a previous study [32]: increased hardness and loss of ductility after aging were observed, while strength values were kept. These changes can be said to be a consequence of the redistribution and chemical evolution of Cr-W-rich precipitates along grain boundaries, combined with the limited plasticity of the Laves phase. The bonding character of the intermetallic phases is neither purely metallic nor completely covalent or ionic, i.e., a certain metallic bond component is always present. These structural features result in a high elastic modulus and a high Peierl stress, so that the intermetallic phases exhibit a high strength. Additionally, the strong bonding forces involved result in a high thermal stability and a high melting point, improving the high temperature strength. Due to the complex atomic configuration, especially the covalent and ionic bonding character, the intermetallic phases exhibit brittle behavior. The ductility is only contributed by the metallic bonding content. A combination of a precipitated intermetallic phase with a ductile mostly ferritic matrix can reduce this typical brittleness. On the other hand, the oxide dispersion distribution in the ODS remains stable after aging, as confirmed by TEM and APT analyses; so, any detrimental effect that might be caused by the intermetallic phases to the mechanical properties seems to be compensated by the stable nanoparticle dispersion. This same explanation is valid to justify the observed DBTT slight displacement from 255±12 K in the ODS reference material to 270±20 K in the ODS aged one [33]. Similar strength values for the ODS alloy before and after the aging treatment seem to be due to

the observed stability of the Y-Ti-O nanoparticle dispersion.

## 5. Conclusions

An ODS steel with composition Fe–14Cr–2W–0.4Ti-0.3$Y_2O_3$ (wt%) has been manufactured by mechanical alloying, compacted by HIP and HCR and thermally aged at 873 K for 2000 h. A thermodynamic simulation of the presence of secondary phases has been performed, together with a multi-technique microstructural characterization by using XRD, EBSD, TEM and APT. From the obtained results, the following conclusions can be extracted:

- Thermodynamic equilibrium simulation predicts stability of Cr-W-rich, Ti-rich and Y-rich precipitates, together with Laves phase formation after aging.
- Stability of the predicted phases is experimentally observed:
  - o $M_{23}C_6$ precipitates are present in the ODS reference material and in the ODS aged material, as confirmed by TEM and EBSD point analysis.
  - o Titanium oxides are observed by TEM before and after aging.
  - o Laves phase seems to have precipitated during aging as, in the ODS aged material, some precipitates located at grain boundaries were identified as Laves phase by XRD, EBSD, TEM and microdiffraction analysis.
  - o A homogeneous distribution of Y-Ti-rich nanoprecipitates inside grains was found by TEM and APT before and after aging. The nanoprecipitates slightly increased in size after aging, but the distance between first neighbor clusters and the (Y+Ti)/O ratio remained unchanged, suggesting stability of the nanoparticle dispersion.
- The microstructural characterization presented here can help explaining the changes observed in the mechanical properties of these same materials analyzed in a previous study [32]: increased hardness, loss of total elongation and a slight shift of the DBTT towards a higher value observed after aging. This behavior can be a consequence of the redistribution and chemical evolution of Cr-W-rich precipitates along grain boundaries, together with Laves phase formation. As the mechanical properties were not dramatically affected, any detrimental effect that may have been caused by the redistribution of precipitates and Laves phase formation seems to have been compensated by the observed stability of the Y-rich nanoprecipitates distribution, which seems to play a main role in the thermal stability of the alloy.

## CRediT authorship contribution statement

**M. Oñoro:** Conceptualization, Data curation, Formal analysis, Investigation, Methodology, Validation, Visualization, Writing – review & editing, Resources. **V. de Castro:** Conceptualization, Data curation, Formal analysis, Funding acquisition, Investigation, Methodology, Resources, Supervision, Validation, Writing – review & editing, Project administration, Visualization. **T. Leguey:** Conceptualization, Data curation, Formal analysis, Investigation, Methodology, Resources, Supervision, Validation, Writing – review & editing, Funding acquisition, Project administration, Visualization. **J. Pöpperlová:** Conceptualization, Data curation, Formal analysis, Investigation, Methodology, Writing – review & editing, Resources, Validation, Visualization. **R.M. Huizenga:** Data curation, Formal analysis, Investigation, Methodology, Resources, Writing – review & editing. **M.A. Auger:** Conceptualization, Data curation, Formal analysis, Funding acquisition, Investigation, Methodology, Project administration, Resources, Supervision, Validation, Visualization, Writing – original draft.

## Declaration of Competing Interest

The authors declare that they have no known competing financial interests or personal relationships that could have appeared to influence the work reported in this paper.

## Data availability

Data will be made available on request.

## Acknowledgements

Funding from AEI (Agencia Estatal de Investigación) with reference AEI/10.13039/501100011033 (project PID2019-105325RB-C33); Comunidad de Madrid (Spain) through the programs Talento-CAM (2017-T1/IND-5439 and 2021-5A/IND-20954), Technofusion (III) CM (S2018/EMT-4437) and multiannual agreement with UC3M ("Excelencia para el Profesorado Universitario"-EPUC3M14) is gratefully acknowledged. Prof. Dr. Ir. J. Sietsma is acknowledged for facilitating access to the X-ray facility at the Department of Materials Science and Engineering, Delft University of Technology, and for providing constructive comments to this work.

## References

[1] E.E. Bloom, The challenge of developing structural materials for fusion power systems, J. Nucl. Mater. 258–263 (1998) 7–17, https://doi.org/10.1016/S0022-3115(98)00352-3.
[2] S.J. Zinkle, Advanced materials for fusion technology, Fusion Eng. Des. 74 (2005) 31–40, https://doi.org/10.1016/j.fusengdes.2005.08.008.
[3] R.L. Klueh, A.T. Nelson, Ferritic/martensitic steels for next-generation reactors, J. Nucl. Mater. 371 (2007) 37–52, https://doi.org/10.1016/j.jnucmat.2007.05.005.
[4] S.J. Zinkle, J.T. Busby, Structural materials for fission & fusion energy, Mater. Today 12 (2009) 12–19, https://doi.org/10.1016/S1369-7021(09)70294-9.
[5] R.J. Kurtz, G.R. Odette, Chapter 3 - overview of reactor systems and operational environments for structural materials in fusion reactors, in: G.R. Odette, S.J. Zinkle (Eds.), Struct. Alloys Nucl. Energy Appl., Elsevier, Boston, 2019, pp. 51–102, https://doi.org/10.1016/B978-0-12-397046-6.00003-4.
[6] S.J. Zinkle, N.M. Ghoniem, Operating temperature windows for fusion reactor structural materials, Fusion Eng. Des. 51–52 (2000) 55–71, https://doi.org/10.1016/S0920-3796(00)00320-3.
[7] R. Alba, R. Iglesias, M. Angeles Cerdeira, Materials to be used in future magnetic confinement fusion reactors: A Review, Materials 15 (2022), https://doi.org/10.3390/ma15196591.
[8] R. Lässer, N. Baluc, J.-L. Boutard, E. Diegele, S. Dudarev, M. Gasparotto, A. Möslang, R. Pippan, B. Riccardi, B. van der Schaaf, Structural materials for DEMO: the EU development, strategy, testing and modelling, Fusion Eng. Des. 82 (2007) 511–520, https://doi.org/10.1016/j.fusengdes.2007.06.031.
[9] E.E. Bloom, S.J. Zinkle, F.W. Wiffen, Materials to deliver the promise of fusion power – progress and challenges, J. Nucl. Mater. 329–333 (2004) 12–19, https://doi.org/10.1016/j.jnucmat.2004.04.141.
[10] G.R. Odette, M.J. Alinger, B.D. Wirth, Recent developments in irradiation-resistant steels, Annu. Rev. Mater. Res. 38 (2008) 471–503, https://doi.org/10.1146/annurev.matsci.38.060407.130315.
[11] T. Hayashi, P.M. Sarosi, J.H. Schneibel, M.J. Mills, Creep response and deformation processes in nanocluster-strengthened ferritic steels, Acta Mater. 56 (2008) 1407–1416, https://doi.org/10.1016/j.actamat.2007.11.038.
[12] J. Hoffmann, M. Rieth, R. Lindau, M. Klimenkov, A. Möslang, H.R.Z. Sandim, Investigation on different oxides as candidates for nano-sized ODS particles in reduced-activation ferritic (RAF) steels, J. Nucl. Mater. 442 (2013) 444–448, https://doi.org/10.1016/j.jnucmat.2013.09.008.
[13] G.R. Odette, N.J. Cunningham, T. Stan, M.E. Alam, Y. De Carlan, Chapter 12 - Nano-oxide dispersion-strengthened steels, in: G.R. Odette, S.J. Zinkle (Eds.), Struct. Alloys Nucl. Energy Appl, Elsevier, Boston, 2019, pp. 529–583, https://doi.org/10.1016/B978-0-12-397046-6.00012-5.
[14] S. Ukai, M. Fujiwara, Perspective of ODS alloys application in nuclear environments, J. Nucl. Mater. 307–311 (2002) 749–757, https://doi.org/10.1016/S0022-3115(02)01043-7.
[15] P. He, R. Lindau, A. Moeslang, H.R.Z. Sandim, The influence of thermomechanical processing on the microstructure and mechanical properties of 13.5Cr ODS steels, Proc. 27th Symp. Fusion Technol. SOFT-27 Liège Belg. Sept. 24–28 2012 88, 2013, pp. 2448–2452, https://doi.org/10.1016/j.fusengdes.2013.04.005.
[16] N. Baluc, J.L. Boutard, S.L. Dudarev, M. Rieth, J.B. Correia, B. Fournier, J. Henry, F. Legendre, T. Leguey, M. Lewandowska, R. Lindau, E. Marquis, A. Muñoz, B. Radiguet, Z. Oksiuta, Review on the EFDA work programme on nano-structured ODS RAF steels, J. Nucl. Mater. 417 (2011) 149–153, https://doi.org/10.1016/j.jnucmat.2010.12.065.
[17] D.T. Hoelzer, J. Bentley, M.A. Sokolov, M.K. Miller, G.R. Odette, M.J. Alinger, Influence of particle dispersions on the high-temperature strength of ferritic alloys, Proc. Twelfth Int. Conf. Fusion React. Mater. ICFRM-12 (367–370) (2007) 166–172, https://doi.org/10.1016/j.jnucmat.2007.03.151.

[18] S.J. Zinkle, L.L. Snead, Designing radiation resistance in materials for fusion energy, Annu. Rev. Mater. Res. 44 (2014) 241–267, https://doi.org/10.1146/annurev-matsci-070813-113627.
[19] V. de Castro, T. Leguey, M. Auger, S. Lozano-Perez, M. Jenkins, Analytical characterization of secondary phases and void distributions in an ultrafine-grained ODS Fe-14Cr model alloy, J. Nucl. Mater. 417 (2011) 217–220, https://doi.org/10.1016/j.jnucmat.2010.12.067.
[20] S. Zinkle, J. Boutard, D. Hoelzer, A. Kimura, R. Lindau, G. Odette, M. Rieth, L. Tan, H. Tanigawa, Development of next generation tempered and ODS reduced activation ferritic/martensitic steels for fusion energy applications, Nucl. Fusion 57 (2017), https://doi.org/10.1088/1741-4326/57/9/092005.
[21] D. Pazos, A. Cintins, V. de Castro, P. Fernández, J. Hoffmann, W.G. Vargas, T. Leguey, J. Purans, A. Anspoks, A. Kuzmin, I. Iturriza, N. Ordás, ODS ferritic steels obtained from gas atomized powders through the STARS processing route: reactive synthesis as an alternative to mechanical alloying, Nucl. Mater. Energy. 17 (2018) 1–8, https://doi.org/10.1016/j.nme.2018.06.014.
[22] S. Bhowmik, P. Varshney, O.E. Atwani, S.A. Maloy, K. Kandasamy, N. Kumar, Assessing manufacturability of the oxide dispersion strengthened (ODS) 14YWT alloy fuel cladding tube using SolidStirTM technology, in: Y. Hovanski, Y. Sato, P. Upadhyay, A.A. Naumov, N. Kumar (Eds.), Frict. Stir Weld. Process, XII, Springer Nature, Switzerland, Cham, 2023, pp. 89–98, https://doi.org/10.1007/978-3-031-22661-8_8.
[23] M.B. Wilms, S.-K. Rittinghaus, M. Goßling, B. Gökce, Additive manufacturing of oxide-dispersion strengthened alloys: materials, synthesis and manufacturing, Prog. Mater. Sci. 133 (2023), 101049, https://doi.org/10.1016/j.pmatsci.2022.101049.
[24] G.A. Cottrell, A survey of plasma facing materials for fusion power plants, Mater. Sci. Technol. 22 (2006) 869–880, https://doi.org/10.1179/174328406X111110.
[25] G. Federici, W. Biel, M.R. Gilbert, R. Kemp, N. Taylor, R. Wenninger, European DEMO design strategy and consequences for materials, Nucl. Fusion 57 (2017), 092002, https://doi.org/10.1088/1741-4326/57/9/092002.
[26] B.C. Maji, S. Ukai, N. Oono-Hori, Microstructural stability and intermetallic embrittlement in high Al containing FeCrAl-ODS alloys, Mater. Sci. Eng. A 807 (2021), 140858, https://doi.org/10.1016/j.msea.2021.140858.
[27] Q. Min, Q. Guo-xing, C. Ming-chong, D. Qing, C. Lei, W. Hong-yan, Microstructure stability and mechanical properties of reduced activated ferritic martensitic steel during thermal aging at 550 °C for 5000 h, J. Mater. Eng. Perform. (2022), https://doi.org/10.1007/s11665-022-07498-6.
[28] P. Zheng, Y. Li, J. Zhang, J. Shen, T. Nagasaka, T. Muroga, H. Abe, On the thermal stability of a 9Cr-ODS steel aged at 700 °C up to 10000 h - mechanical properties and microstructure, Mater. Sci. Eng. A 783 (2020), 139292, https://doi.org/10.1016/j.msea.2020.139292.
[29] B.R. Sun, A.D. Zhou, Y.L. Li, Z.L. Zhang, C.C. Du, S.X.Y. Gu, Z. Chen, X.C. Cai, S. W. Xin, T.D. Shen, Ultrafine-grained oxide-dispersion-strengthened 9Cr steel with exceptional strength and thermal stability, Nucl. Mater. Energy. 30 (2022), 101112, https://doi.org/10.1016/j.nme.2021.101112.
[30] P.-L. Gao, J. Gong, Q. Tian, G.-A. Sun, H.-Y. Yan, L. Chen, L.-F. Bai, Z.-M. Guo, X. Ju, Small-angle neutron scattering study on the stability of oxide nanoparticles in long-term thermally aged 9Cr-oxide dispersion strengthened steel, Chin. Phys. B 31 (2022), 056102, https://doi.org/10.1088/1674-1056/ac43aa.
[31] Y.R. Wen, Y. Liu, D.H. Liu, B. Tang, Preparation and thermal stability of a mechanically alloyed oxide dispersion strengthened ferritic steels, Mater. Sci. Forum 715–716 (2012) 605–610, https://doi.org/10.4028/www.scientific.net/MSF.715-716.605.
[32] M. Oñoro, J. Macias-Delgado, M.A. Auger, V. de Castro, T. Leguey, Mechanical properties and stability of precipitates of an ODS steel after thermal cycling and aging, Nucl. Mater. Energy 24 (2020), https://doi.org/10.1016/j.nme.2020.100758.
[33] M. Oñoro, T. Leguey, V. de Castro, M.A. Auger, Effects of thermal aging at 873K on the impact properties of an ODS ferritic steel, Nucl. Mater. ENERGY. (2023), https://doi.org/10.1016/j.nme.2023.101455.
[34] J. Macías-Delgado, Microestructura y propiedades mecánicas de aceros de activación reducida endurecidos mediante dispersión de óxidos, Universidad Carlos III de Madrid, 2019. http://hdl.handle.net/10016/29747.
[35] H.L. Lukas, S.G. Fries, B. Sundman, Computational Thermodynamics: The Calphad Method, Cambridge University Press, Cambridge, UK, 2007, https://doi.org/10.1017/CBO9780511804137.
[36] Digital MicrographTM, (n.d.). https://www.gatan.com/products/tem-analysis/digitalmicrograph-software.
[37] W.S. Rasband, ImageJ, (n.d.). https://imagej.net/ij/index.html.
[38] M.K. Miller, K.F. Russell, Atom probe specimen preparation with a dual beam SEM/FIB miller, Ultramicroscopy. 107 (2007) 761–766, https://doi.org/10.1016/j.ultramic.2007.02.023.
[39] M.K. Miller, Atom Probe Field Ion Microscopy, Clarendon Press, Oxford, 1996.
[40] B. Gault, M.P. Moody, J.M. Cairney, S.P. Ringer, Atom probe microscopy, Springer, New York, 2012. https://link.springer.com/book/10.1007/978-1-4614-3436-8.
[41] Cameca IVAS, (n.d.). https://www.cameca.com/service/software/ivas.
[42] A. Machida, H. Saitoh, T. Hattori, A. Sano-Furukawa, K. Funakoshi, T. Sato, S. Orimo, K. Aoki, Hexagonal close-packed Iron hydride behind the conventional phase diagram, Sci. Rep. 9 (2019) 12290, https://doi.org/10.1038/s41598-019-48817-7.
[43] H. Arnfelt, A. Westgren, Crystal structure and composition of the intermediate phases present in iron-tungsten and iron-molybdenum alloys, Jernkontorets Ann. 119 (1935) 184–196.
[44] M. Oñoro, J. Macías-Delgado, M.A. Auger, J. Hoffmann, V. de Castro, T. Leguey, Powder particle size effects on microstructure and mechanical properties of mechanically alloyed ODS ferritic steels, Metals. 12 (2022), https://doi.org/10.3390/met12010069.
[45] M. Klinger, More features, more tools, more CrysTBox, J. Appl. Crystallogr. 50 (2017) 1226–1234, https://doi.org/10.1107/S1600576717006793.
[46] Q. Li, Precipitation of Fe2W laves phase and modeling of its direct influence on the strength of a 12Cr-2W steel, Metall. Mater. Trans. -Phys. Metall, Mater. Sci. 37A (2006) 89–97, https://doi.org/10.1007/s11661-006-0155-2.
[47] K. Yamamoto, Y. Kimura, Y. Mishima, Effect of matrix microstructure on precipitation of laves phase in Fe–10Cr–1.4W(–co) alloys, Intermetallics. 14 (2006) 515–520, https://doi.org/10.1016/j.intermet.2005.09.005.
[48] O. Prat, J. Garcia, D. Rojas, G. Sauthoff, G. Inden, The role of laves phase on microstructure evolution and creep strength of novel 9%Cr heat resistant steels, INTERMETALLICS. 32 (2013) 362–372, https://doi.org/10.1016/j.intermet.2012.08.016.
[49] A. Iwamaru, H. Hisazawa, Y. Terada, Microstructure evolution of Fe-Ni-based alloy HR6W during isothermal aging, Mater. Trans. 60 (2019) 824–829, https://doi.org/10.2320/matertrans.M2019032.
[50] J.M. Cairney, K. Rajan, D. Haley, B. Gault, P.A.J. Bagot, P.-P. Choi, P.J. Felfer, S. P. Ringer, R.K.W. Marceau, M.P. Moody, Mining information from atom probe data, 1st Int, Conf. At. Probe Tomogr. Microsc. 159 (2015) 324–337, https://doi.org/10.1016/j.ultramic.2015.05.006.
[51] M.K. Michael, K. Miller, Atom probe tomography: analysis at the atomic level, Kluwer Academic / Plenum Publishers, New York, New York, 2000.
[52] C.A. Williams, D. Haley, E.A. Marquis, G.D.W. Smith, M.P. Moody, Defining clusters in APT reconstructions of ODS steels, IFES 2012 (132) (2013) 271–278, https://doi.org/10.1016/j.ultramic.2012.12.011.
[53] M.K. Miller, R. Forbes, Atom Probe Tomography : The Local Electrode Atom Probe, Springer, New York, 2014.
[54] M. Miller, E. Kenik, Atom probe tomography: a technique for nanoscale characterization, Microsc. Microanal. 10 (2004) 336–341, https://doi.org/10.1017/S1431927604040577.
[55] V. Knežević, J. Balun, G. Sauthoff, G. Inden, A. Schneider, Design of martensitic/ferritic heat-resistant steels for application at 650°C with supporting thermodynamic modelling, in: 3rd Int. Conf. Spray Depos. Melt At. SDMA 2006 6th Int. Conf. Spray Form. ICSF VI 477, 2008, pp. 334–343, https://doi.org/10.1016/j.msea.2007.05.047.
[56] C.G. Panait, W. Bendick, A. Fuchsmann, A.-F. Gourgues-Lorenzon, J. Besson, Study of the microstructure of the grade 91 steel after more than 100,000 h of creep exposure at 600 °C, Int. J. Press. Vessel. Pip. 87 (2010) 326–335, https://doi.org/10.1016/j.ijpvp.2010.03.017.
[57] W. Yan, W. Wang, Y.-Y. Shan, K. Yang, Microstructural stability of 9–12%Cr ferrite/martensite heat-resistant steels, front, Mater. Sci. 7 (2013) 1–27, https://doi.org/10.1007/s11706-013-0189-5.
[58] D.A. Porter, Phase transformations in metals and alloys, 2nd ed., [reprint.], Chapman & Hall, London, 1993.
[59] M.K. Miller, D.T. Hoelzer, E.A. Kenik, K.F. Russell, Stability of ferritic MA/ODS alloys at high temperatures, Intermetallics. 13 (2005) 387–392, https://doi.org/10.1016/j.intermet.2004.07.036.
[60] X.L. Wang, C.T. Liu, U. Keiderling, A.D. Stoica, L. Yang, M.K. Miller, C.L. Fu, D. Ma, K. An, Unusual thermal stability of nano-structured ferritic alloys, J. Alloys Compd. 529 (2012) 96–101, https://doi.org/10.1016/j.jallcom.2012.02.143.